

## Article

# Carbon-Free Cathode Materials Based on Titanium Compounds for Zn-Oxygen Aqueous Batteries

Jorge González-Morales <sup>1</sup>, Jadra Mosa <sup>1,\*</sup>, Sho Ishiyama <sup>2</sup>, Nataley Carolina Rosero-Navarro <sup>1,2</sup>, Akira Miura <sup>2</sup>, Kiyoharu Tadanaga <sup>2</sup> and Mario Aparicio <sup>1</sup>

<sup>1</sup> Instituto de Cerámica y Vidrio (ICV-CSIC), c/ Kelsen 5, Campus de Cantoblanco, 28049 Madrid, Spain; jorge.gonzalez.morales@icv.csic.es (J.G.-M.); rosoro@icv.csic.es (N.C.R.-N.); maparicio@icv.csic.es (M.A.)

<sup>2</sup> Department of Applied Chemistry, Faculty of Engineering, Hokkaido University, Sapporo 060-8628, Japan; ish\_5000d10@eis.hokudai.ac.jp (S.I.); amiura@eng.hokudai.ac.jp (A.M.); tadanaga@eng.hokudai.ac.jp (K.T.)

\* Correspondence: jmossa@icv.csic.es

**Abstract:** The impact of global warming has required the development of efficient new types of batteries. One of the most promising is Zn-O<sub>2</sub> batteries because they provide the second biggest theoretical energy density, with relevant safety and a cycle of life long enough to be fitted for massive use. However, their industrial use is hindered by a series of obstacles, such as a fast reduction in the energy density after the initial charge and discharge cycles and a limited cathode efficiency or an elevated overpotential between discharge and charge. This work is focused on the synthesis of titanium compounds as catalysts for the cathode of a Zn-O<sub>2</sub> aqueous battery and their characterization. The results have shown a surface area of 350 m<sup>2</sup>/g after the elimination of the organic templates during heat treatment at 500 °C in air. Different thermal treatments were performed, tuning different parameters, such as intermediate treatment at 500 °C or the atmosphere used and the final temperature. Surface areas remain high for samples without an intermediate temperature step of 500 °C. Raman spectroscopy studies confirmed the nitridation of samples. SEM and XRD showed macro-meso-porosity and the presence of nitrogen, and the electrochemical evaluation confirmed the catalytic properties of this material in oxygen reaction reduction (ORR)/oxygen evolution reaction (OER) analysis and Zn-O<sub>2</sub> battery tests.



**Citation:** González-Morales, J.; Mosa, J.; Ishiyama, S.; Rosero-Navarro, N.C.; Miura, A.; Tadanaga, K.; Aparicio, M. Carbon-Free Cathode Materials Based on Titanium Compounds for Zn-Oxygen Aqueous Batteries. *Batteries* **2024**, *10*, 94. <https://doi.org/10.3390/batteries10030094>

Academic Editor: Xianyong Wu

Received: 23 January 2024

Revised: 23 February 2024

Accepted: 28 February 2024

Published: 6 March 2024



**Copyright:** © 2024 by the authors. Licensee MDPI, Basel, Switzerland. This article is an open access article distributed under the terms and conditions of the Creative Commons Attribution (CC BY) license (<https://creativecommons.org/licenses/by/4.0/>).

## 1. Introduction

Carbon dioxide levels in the atmosphere are exceeding the average of 410 ppm, and the lack of significant changes in human dependence on fossil fuels for transportation and other activities is forcing the development of more efficient methods of energy storage [1]. Batteries permit chemical energy storage and its efficient conversion into electrical energy. Secondary batteries have the advantage of being able to be reused in multiple cycles of charge and discharge, having a lower ecological impact [2,3].

The global transition to a carbon-free energy model requires extensive changes in transportation: an energy source with high energy density and volume limitations that up-to-date generations of batteries cannot meet [4]. Nowadays, there is a steady increase in the demand for rechargeable batteries in transport sectors, such as personal transport vehicles, airplanes, or other models of transportation. Consequently, this has led to highlighting the weaknesses or failures of metal-ion batteries, mainly due to their low energy density, which makes their widespread use in locomotion very challenging [5]. This has led to the introduction of new types of batteries with a higher energy density that allow to reduce the volume used by current batteries as well as reduce and optimize the demand for a scarce resource, such as noble metals [6]. Therefore, the need to develop batteries that combine environmental sustainability, security, chemical stability, and energy density comparable to

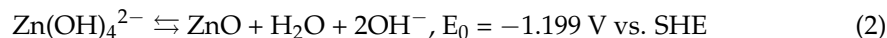
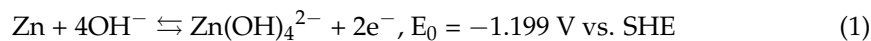
conventional energy sources has driven new developments in the field, such as metal-air batteries [7].

Metal-air batteries have received attention due to their high theoretical energy density, mainly for use in transportation. However, they are in a fundamental research step due to several inconveniences, such as the use of a metallic anode and the tendency to form dendrites that shorten the useful charge and discharge cycles of the battery [5,6]. Metal-air batteries can be classified depending on the medium by which the metal reacts with O<sub>2</sub> in aqueous and non-aqueous batteries. In non-aqueous batteries, the metal reacts with oxygen that is reduced, presenting a lower tendency toward electrolyte corrosion but higher resistance to electrolyte carbonation processes and a longer theoretical life cycle than its aqueous counterpart [8]. Regarding aqueous batteries, they offer a series of advantages, such as greater safety, the absence of a solid electrolyte, allowing a reduction in costs, and better contact between the metallic ions and the oxygen [9,10].

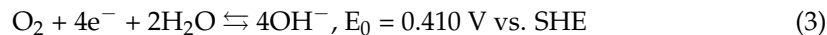
Another inconvenience is that sometimes, oxygen can enter the cell and react with the electrolyte with a lack of input during operation [11]. The metallic anode can be made of multiple elements, such as Li, Na, K, Zn, Al, Mg, and Fe [4]. Within the metal-air batteries, Li-air batteries have the highest energy density, around 5200 Wh kg<sup>-1</sup>. Zn-air batteries have the advantage of being more affordable due to the high cost of Li and safer due to the high flammability and reactivity of Li, although Zn batteries have a lower energy density than Li-air batteries [9,12,13]. One of the determining factors in the performance of batteries is the products generated during their operational life, which change significantly depending on the electrolyte used. In non-aqueous metal-air batteries, metal oxides are rapidly generated, allowing high potentials and a high energy density, but these oxides require a higher potential to be decomposed, and this overpotential is a problem that limits the energy efficiency of these batteries [14]. However, in aqueous metal-air batteries, the hydroxide ions are generated at the cathode from oxygen reduction (ORR) and the metal ions react to form a metal hydroxide in the discharge process [15]. This metal hydroxide is less stable than the metal oxide, which allows the overpotentials involved to be lower than those in non-aqueous batteries [16].

In Zn-O<sub>2</sub> batteries, a series of reactions take place thanks to the constant supply of oxygen. The main sequence of reactions in a Zn battery using aqueous electrolytes during the discharge process are:

Zn electrode:



Air electrode or cathode:



Global reaction:



The charge process includes the decomposition of the Zn hydroxides–oxides, generating the reduction of the metal and the oxygen evolution reaction (OER).

The path leading to improved batteries with bigger energy and power densities has implied approaches, such as the use of carbon-based materials on the gas diffusion layer and as a substrate for catalysts based on their high conductivity and surface area. However, these carbon-based electrodes suffer from corrosion at high potentials during the battery charging process (OER), since even at the open-circuit potential of Zn-O<sub>2</sub> batteries, the process is thermodynamically favorable [17]. These problems, involved in the use of carbon in batteries, have led to the development of different materials as substitutes [18,19], and various options have been studied, such as cathodes supported on Ni foams or the use of metallic nanoparticles [20–22].

The research field of the Zn-O<sub>2</sub> batteries is an expanding and cutting-edge one. As far as the cathodes are concerned, multiple strategies are being developed, such as the use of 3D graphene structures [10,23], CoO/CoP heterostructures [24], manganese nitride [25], NiCo<sub>2</sub>O<sub>4</sub>@FeNi LDH [26], PtPd alloys [27], titanium carbide [28], or molecular catalysts [29], aiming to obtain more efficient cathodes with a longer life cycle and reducing the dependence on strategic materials. A review concerning the development of electrodes for Zn-air batteries was recently published [30]. Another route of research is the synthesis of transition metal nitrides, such as titanium, as catalysts for the cathodes. Moreover, oxynitrides have been used in different types of batteries, such as Li-air, Li-S, and other metal-air batteries, to improve the electrochemical performance, extend the number of stable charge-discharge cycles, provide better reactivity at the ORR [27], and for better corrosion resistance or improved morphological properties of the cathode, such as its porosity or surface area [31–35].

In this paper, a novel bifunctional titanium-based catalyst deposited onto Ni foam was prepared as a cathode for rechargeable aqueous Zn-O<sub>2</sub> batteries. Optimization of thermal treatments to obtain crystalline porous materials with an adequate surface area and morphology was performed in order to enhance the catalyst performance. A proper design of ORR and OER bifunctional catalysts allows an excellent performance and good long-term stability (over 300 h). Herein, we developed a facile approach to processing ceramic titanium compounds with balanced OER and ORR catalytic activities utilized as the air electrode for aqueous Zn-O<sub>2</sub> batteries.

## 2. Materials and Methods

Titanium-based catalysts for cathode aqueous Zn-O<sub>2</sub> batteries were prepared through the sol-gel process, wherein at the first stage, 0.30 g of Triton X-100 (Aldrich, St. Quentin Fallavier, France, 98%) was dissolved in 12 g of tetrahydrofuran (THF; Aldrich, 99.9%) at room temperature. Once the Triton was completely dissolved, 0.45 g of TEOS (Aldrich, 98%) was added under stirring at room temperature for 10 min (Figure 1). Then, 0.75 g of titanium (IV) isopropoxide (Aldrich, 97%) was added under stirring. Once the titanium (IV) isopropoxide was completely dissolved, 0.30 g of a previously synthesized Resol resin [30] was added under stirring at room temperature for half an hour, and then the pH was adjusted by slowly dripping 0.90 g of HCl (Aldrich, 37%). Finally, the solution was stirred for one hour, after which the final product was transferred to a Petri dish.

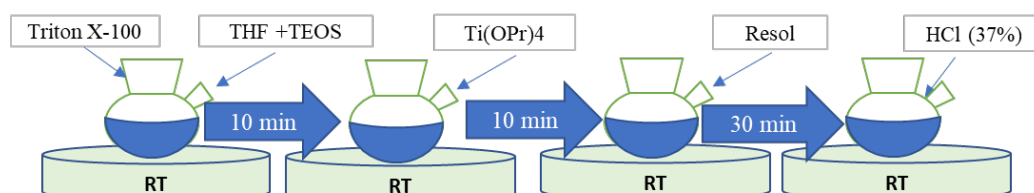


**Figure 1.** Synthesis flow chart.

The Resol resin was previously synthesized, melting 3.054 g of phenol (99–100.5%) at 42 °C and adding 0.656 g of NaOH 20% mass/volume under stirring. After that, 5.25 g of formaldehyde was added at 70 °C, and after cooling, the pH was adjusted with HCl (37%) to a pH of 7. Then, after 24 h, 26 mL of THF (99.9%) was added under stirring, and vacuum-filtered with a 5–13 µm filter. The filtrate was re-filtered with a 0.45 µm syringe filter and, finally, the resin was dried using an oven at 40 °C.

The final product was subjected to a series of thermal treatments at different temperatures to obtain a ceramic material with porosity and surface area. First, a heat treatment at 100 °C for 12 h was performed to remove THF and HCl, and then the samples were ground on an agate mortar. After the thermal treatment at 100 °C, the samples were heat-treated using two alternative high-temperature thermal treatments: (a) A 2-step treatment, where the samples were first heated at 500 °C in air, and then at 800, 900, or 1000 °C in a flow of NH<sub>3</sub>, namely 500–800-NH<sub>3</sub>, 500–900-NH<sub>3</sub>, and 500–1000-NH<sub>3</sub>, respectively. (b) Samples

that were subjected directly to a thermal treatment at 800 °C in a flow of N<sub>2</sub> or NH<sub>3</sub>, namely 800-N<sub>2</sub> and 800-NH<sub>3</sub>.

After that, TEOS was removed by adding 10 mL of 1 M NaOH to the powder, subjected to ultrasonic agitation for 30 min, and centrifuged at 2000 rpm for 15 min. The process was repeated 3 times to eliminate the supernatant liquid. Finally, the process was repeated another 3 times with distilled water instead of 1 M NaOH and the final product was dried at 80 °C for 24 h.

Thermogravimetric analysis (TGA) and differential thermal analysis (DTA) were performed on 21.916 mg of the sample previously treated at 100 °C with a Netzsch, Selb, Germany, STA 409/C equipped between 25 °C and 800 °C, increasing the temperature by 5 °C per minute. The composition and morphology of the sample were studied with a field emission scanning electron microscope (FE-SEM; Hitachi S-4700, Tokyo, Japan) at 20 kV, coupled to an energy-dispersive X-ray (EDX) spectroscopy system (NORAN system). The surface area of the samples was measured through the Brunauer–Emmett–Teller (BET) method in a Quanta Chrome model Monosorb after 2 h of degassing at 150 °C in argon flow. The FTIR analysis was performed on the powder of ground samples using a Perkin Elmer Spectrum 100, Waltham, MA, USA, with a PIKE GladiATR accessory.

Samples were characterized using confocal Raman spectroscopy using a WITec alpha-300R model, Oxford Instruments, Abingdon, UK. A laser with an excitation wavelength of 532 nm was used to recorded spectra. Areas of 10 × 10 μm at different integration times were studied. The power of the incident laser was 0.3 mW. The resolution for the Raman spectra was 0.02 cm<sup>-1</sup> and the optical resolution of the confocal microscope was limited to ~200 nm laterally and 500 nm vertically. Spectra were analyzed and processed through the program WITEC 2.02 Project.

The phase analysis was carried out using X-ray diffraction (XRD) in a Bruker, Billerica, MA, USA, D8 Advance with a CoK $\alpha$  radiation source ( $k = 0.178797$  nm), and the software used for the data interpretation was DIFFRAC.EVA version 6. The determination of the crystallite size was realized by the application of the Scherrer equation at the peak at 62°. Electrochemical measurements were performed with a potentiostat Solartron 1287 (Solartron Analytical, Farnborough, UK) to evaluate ORR and OER using a three-electrode system. The working electrode was the Ti-based catalyst supported on a Ni foam, a platinum wire was used as a counter electrode, and a Hg/HgO electrode as a reference electrode. The measurements were performed in 1 M KOH electrolyte. Two-electrode battery tests were performed using PAT-Cell-Gas (EL-CELL, Harburg, Germany) with a pure oxygen flow and a bilayer polypropylene/polyethylene membrane as a separator, using a Multichannel Potentiostat VMP3 (Biologic, Seyssinet-Pariset, France). The cathode ink was prepared by mixing 10 mg of catalyst, 0.3 mL of Nafion solution (5%), and 50 μL of ethanol. The ink was applied on the 18 mm-diameter, circular Ni foam (Recemat BV, Dodewaard, The Netherlands) as a working electrode and vacuum-dried at 80 °C. A polished Zn foil (counter and reference electrodes) was used as an anode and 300 μL of 6 M KOH as an electrolyte. Cyclic voltammetry measurements were performed using a two-electrode system between 0.9 and 2.2 V vs. Zn with a scan rate of 50 mV/min. Galvanostatic charge–discharge tests were carried out between 0.9 and 2.2 V vs. Zn with a current density of 5 mA/cm<sup>2</sup>. During the test, the maximum potential (2.2 V) was reduced to 1.9 V vs. Zn.

### 3. Results

#### *Structural Characterization*

The sample heat-treated at 100 °C in air presented a whitish appearance, characteristic of materials obtained from titanium alkoxides, while the samples treated at higher temperatures changed to a dark black color, characteristic of nitrogen- and carbon-containing compounds.

The TGA and DTA analyses were performed on the powder treated at 100 °C using a heating ramp of 5 °C/min. Figure 2 shows the variations in sample weight and the heat

flow from 25 °C to 800 °C. Three different regions were observed. The first one (R.I), until 150 °C with an 8% weight, corresponded to a small endothermic peak at 60 °C related to the elimination of water and residual solvents coming from sol synthesis. The second region (R.II), between 150 °C and 480 °C, presented a weight reduction of 55% due to the decomposition of the organic templates and organic chains from precursors [36]. Finally, in R.III, above 480 °C, no significant changes in weight (2%) were observed. In conclusion, the TGA curves showed that 500 °C is an adequate intermediate thermal treatment in order to remove surfactants and organic residues from unhydrolyzed ligands.

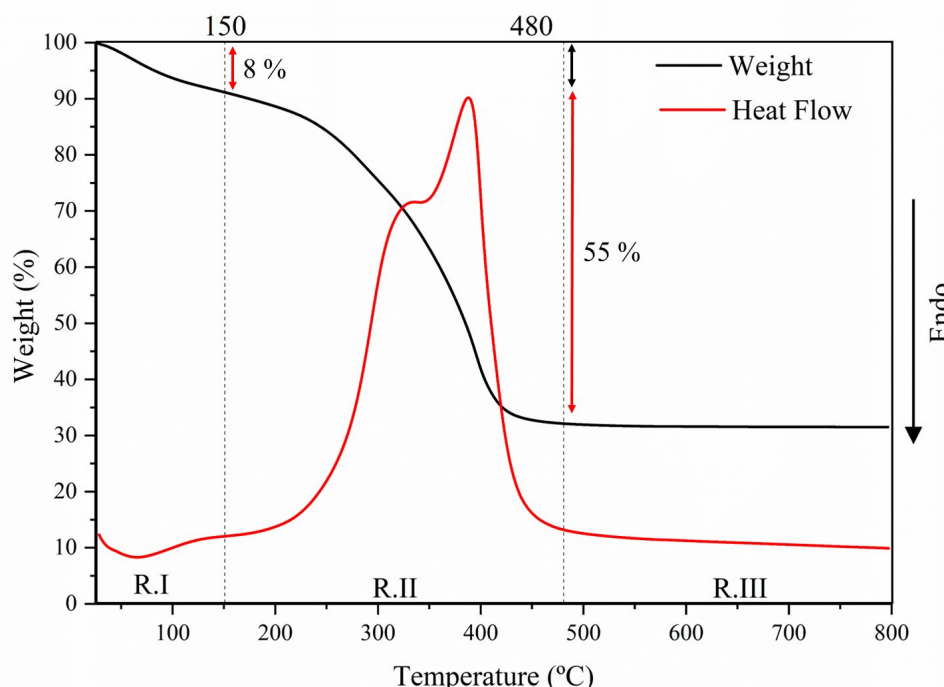


**Figure 2.** Thermogravimetric analysis (TGA) and differential thermal analysis (DTA) of a sample thermal-treated at 100 °C in air.

Table 1 shows the surface area and electric conductivity of the sample under different thermal treatments and atmospheres.

**Table 1.** Specific surface area and electrical conductivity of the different samples analyzed.

Sample	Surface Area ( $\text{m}^2/\text{g}$ )	Electric Conductivity ( $\text{mS}/\text{cm}$ )
100-air	0.1	$3 \times 10^{-7}$
500-air	347	---
500–800-NH <sub>3</sub>	3.3	0.97
500–900-NH <sub>3</sub>	4.9	---
500–1000-NH <sub>3</sub>	1.7	1.4
800-N <sub>2</sub>	85	0.97
800-NH <sub>3</sub>	237	0.99

The sample heat-treated at 100 °C presented a low specific surface area and electric conductivity because it still presented surfactants on the material, forming a dense and interpenetrating structure. A remarkable increase in the surface area was observed after thermal treatment at 500 °C ( $347 \text{ m}^2/\text{g}$ ), a temperature at which surfactants are removed, as the ATG curves confirmed, resulting in an increase of the specific surface area. However, the surface areas of samples 500–800-NH<sub>3</sub>, 500–900-NH<sub>3</sub>, and 500–1000-NH<sub>3</sub> suffered a significant decrease in value, at 3.3, 4.9, and  $1.7 \text{ m}^2/\text{g}$ , respectively. This fact could be

due to a collapse of the pores of the samples due to the crystallization of the material, as enhancing the crystal size causes a decrease in the pore sizes [37].

Retention of the open pore volume is critical for maintaining a high surface area, so successful optimization of the thermal treatment is needed. The reduction in the surface area was mitigated by treating the sample directly at a high temperature (800 °C in N<sub>2</sub> or NH<sub>3</sub> atmosphere) after drying at 100 °C. In this case, surface areas of 85 and 237 m<sup>2</sup>/g were obtained for samples 100–800 and 100–900, respectively. Moreover, the electrical conductivity increased by seven orders of magnitude when the sample was heat-treated up to 800 °C, possibly due to the nitridation of the sample [38,39].

The morphological characteristics of the titanium catalysts under different thermal treatments were studied using the SEM technique (Figure 3).

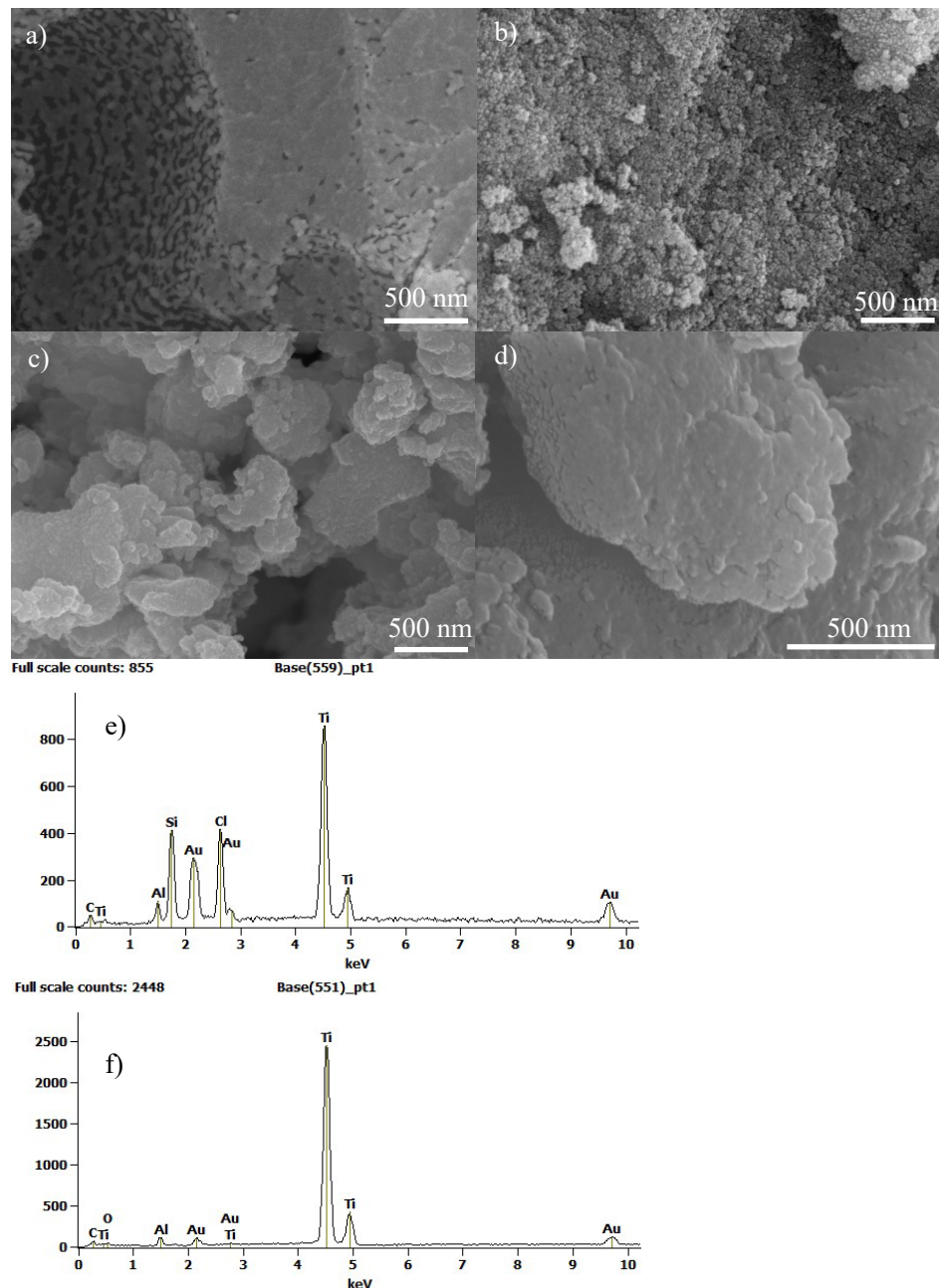


**Figure 3.** SEM images of the titanium samples: (a) 100-air, (b) 500-air, (c) 500–800-NH<sub>3</sub>, and (d) 800-NH<sub>3</sub>, and EDX results: (e) 100-air, and (f) 500-air and silica removal.

Two differentiated phases are observed in Figure 3a, indicating that the sample at 100 °C showed a homogeneous distribution of the inorganic and organic components. EDX spectroscopy (Figure 3e) showed the presence of Ti, Si, and Cl as main components of the sample after this low-temperature thermal treatment. Figure 3b presents a SEM image of the sample after the thermal treatment at 500 °C in air, showing a relevant increase in macro-porosity and meso-porosity as a consequence of surfactant removal. After this thermal treatment and silica removal process, only Ti was shown in the EDX spectra (Figure 3f). A reduction in the porosity is observed in Figure 3c for sample 500–800-NH<sub>3</sub>. Although a consolidation of the porous structure was performed during thermal treatment at 500 °C in air, the subsequent treatment at 800 °C produced a partial collapse of the pores due to crystallization and enhancement of the crystal size. Finally, in Figure 3d, sample 800 °C-NH<sub>3</sub> is observed, confirming the decrease in meso- and macro-porosity; however, it presents microporosity in agreement with the high surface area previously indicated.

FTIR spectra of 500-air, 500–900-NH<sub>3</sub>, and 500–1000-NH<sub>3</sub> catalysts are shown in Figure 4a, and 800-N<sub>2</sub> and 800-NH<sub>3</sub> spectra in Figure 4b.

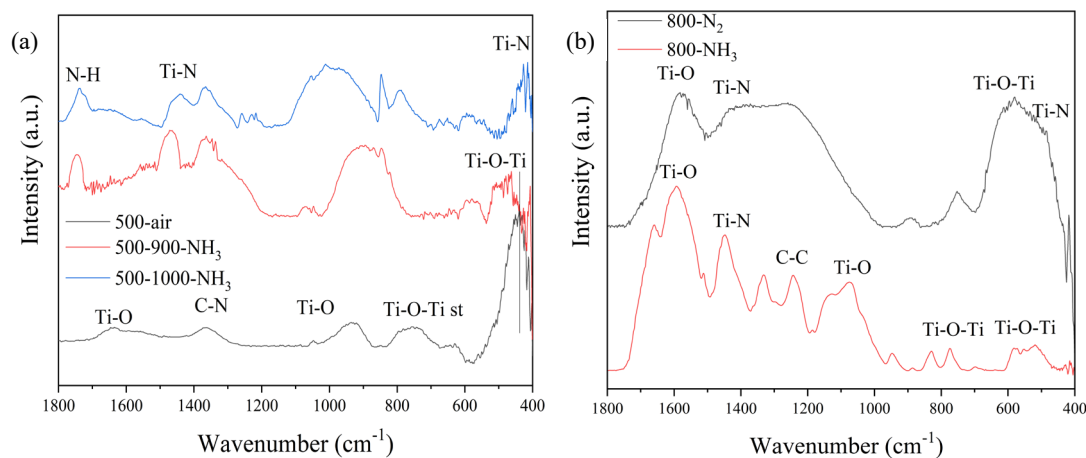


**Figure 4.** (a) FTIR spectra of the samples 500, 500–900-NH<sub>3</sub>, and 500–1000-NH<sub>3</sub>, and (b) FTIR spectra of the samples 800-NH<sub>3</sub> and 800-N<sub>2</sub> in the range 1800–400 cm<sup>-1</sup>.

Sample 500-air did not present peaks related to TiN, and the main absorption bands were related to anatase phase. The band present at 1630 cm<sup>-1</sup> was assigned to Ti-O and was observed only in the 500 °C spectra. Broad bands at 960 and 400 cm<sup>-1</sup> were assigned to Ti-O stretching and Ti-O-Ti bonding stretching modes. The band that appeared at 728 cm<sup>-1</sup> was assigned to Ti-O-Ti stretching vibrations in anatase. The broad peaks indicate the low crystallization of the anatase phase. Additionally, it is possible to observe a band at 1453 cm<sup>-1</sup> that was related to the C-N stretching frequency. Spectra of samples 500–900-NH<sub>3</sub> and 500–1000-NH<sub>3</sub> presented some differences compared with lower temperatures, mainly due to the nitrification of the sample [40]. In the presence of N, the main absorption bands of anatase shifted to slightly higher wavenumbers as the N content increased [41]. This shift was due to the progressive substitution of oxygen atoms by nitrogen ones in the TiO<sub>2</sub> lattice. The small and broad band at 600 cm<sup>-1</sup> was related to TiO<sub>2</sub>-N due to the presence of Ti-N bonds. In both spectra, it was possible to observe a band related to N-H stretching at 1739 cm<sup>-1</sup> and a C-N band at 1453 cm<sup>-1</sup>, as in the previous sample. The band at 418 cm<sup>-1</sup> can be attributed to the formation of N-Ti-N bonds [41–43]. Spectra of samples 800-N<sub>2</sub> and 800-NH<sub>3</sub> presented a broad band at 600 cm<sup>-1</sup> associated with TiO<sub>2</sub>-N and a band at 480 cm<sup>-1</sup> related to N-Ti-N bonds [42], while the band at 1550 cm<sup>-1</sup> and the broad band at 1200–1400 cm<sup>-1</sup> were due to organic groups' C-N and C-C bonds. However, the 800-N<sub>2</sub> catalyst presented a spectrum with fewer bands than 800-NH<sub>3</sub>. Several differences could be observed: a wide band between 1340 and 1250 cm<sup>-1</sup> related to C-C bonds and a band at 780 cm<sup>-1</sup> assigned to the Ti-O bonding stretching mode.

Raman spectroscopy was performed to study the structural composition and crystal phases of the samples. Figure 5 shows (a) an optical Raman spectroscopy image of the 500-air sample and (b) different analyses of spectra in the sample. For all spectra, analysis of the XY surface (white square) and individual analysis points (red and blue crosses) showed only the anatase-TiO<sub>2</sub> phase. There were a series of bands at 144, 195, 393, 517, and 638 cm<sup>-1</sup> related to TiO<sub>2</sub> (anatase) and assigned to A1g + 2B1g + 3Eg active bands in the Raman spectrum.

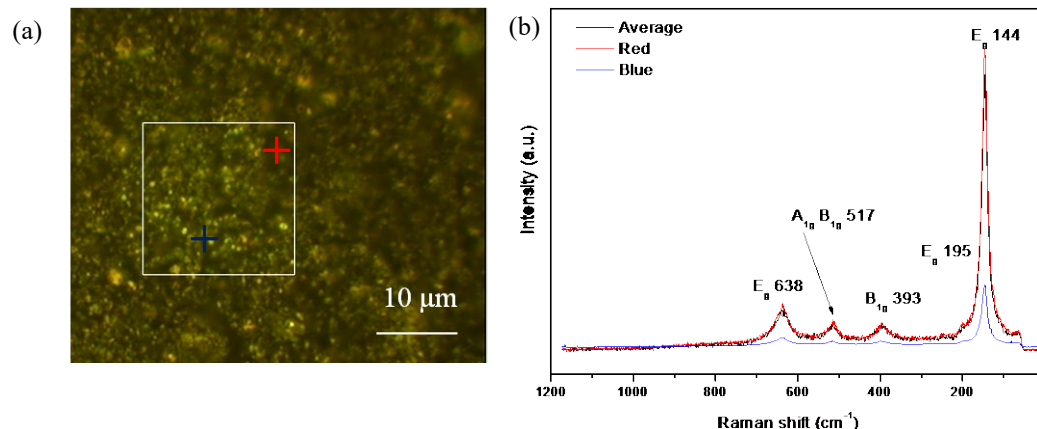


**Figure 5.** (a) Confocal microscopy image and (b) Raman spectrum of the 500-air sample. The white square is the XY surface mapping, represented as the Raman spectra average, and the red and blue crosses represent spectra points.

Figure 6 shows a detailed study of the 500–900-NH<sub>3</sub> catalyst. Figure 6a shows a Raman image obtained from XY superficial mapping, including phase identification, and Figure 6b shows Raman spectra of different integrated phases and average spectra for comparison.

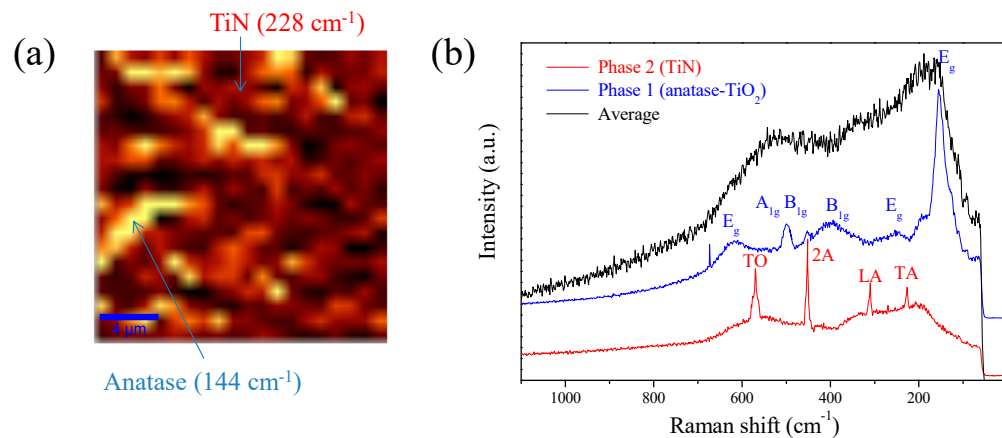
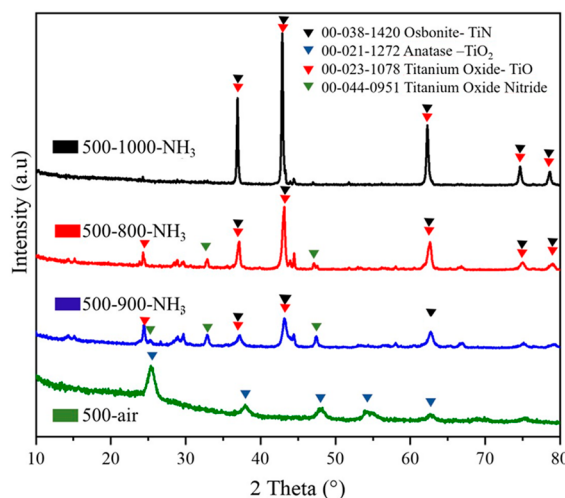


**Figure 6.** Raman analysis for the 500–900-NH<sub>3</sub> catalyst: (a) In-plane Raman intensity image obtained from XY superficial mapping ( $10 \times 10 \mu\text{m}$ ), measuring different single Raman spectra taken each 100 nm with an integration time of 3 s at 0.3 mW (bright areas = anatase and dark areas = TiN). (b) Average Raman spectra obtained from the in-plane Raman image (black), anatase (blue), and TiN (red) were all detected. Main peaks are labeled for both phases.

Analyzing nitrides of Ti via Raman spectroscopy is quite complicated because they present a high conductivity. Optimal acquisition of spectra was possible using a 0.3 mW power laser, avoiding overheating and partial oxidation of TiN. Two well-differentiated phases could be analyzed by surface XY mapping of the surface ( $10 \mu\text{m} \times 10 \mu\text{m}$ ) for 3 s. Raman bands appeared at 144, 195, 393, 517, and 638 cm<sup>-1</sup>, which can be assigned to anatase phase corresponding to A1g + 2B1g + 3Eg active bands for the Raman spectra, as shown in the sample heat-treated at 500 °C [44–46]. The second integrated phase with

phonon frequencies at approximately 228, 310, 452, and 571 cm<sup>-1</sup> was related to transverse acoustic (TA), longitudinal acoustic (LA), second-order acoustic (2A), and transverse optical (TO) modes of TiN, respectively [47]. The Raman image and average spectra confirmed that TiN phase was predominant at 900 °C. This result indicated that TiN phase formed after the sample was nitrided at 900 °C in NH<sub>3</sub> atmosphere, which was consistent with the FTIR results.

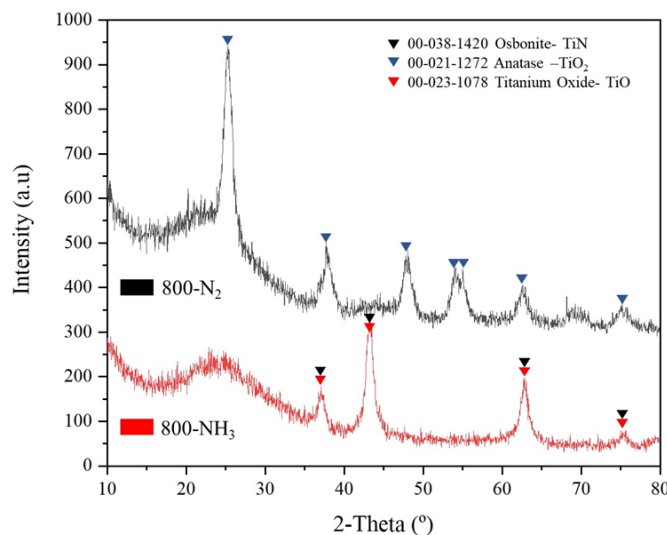
Figure 7 shows X-ray diffractogram profiles of samples 500–800-NH<sub>3</sub>, 500–900-NH<sub>3</sub>, and 500–1000-NH<sub>3</sub>. The intensity of the peaks increased with the temperature, indicating an increase in the crystallinity of the sample.



**Figure 7.** X-ray diffraction patterns of 500-air, 500–800-NH<sub>3</sub>, 500–900-NH<sub>3</sub>, and 500–1000-NH<sub>3</sub> catalyst powders.

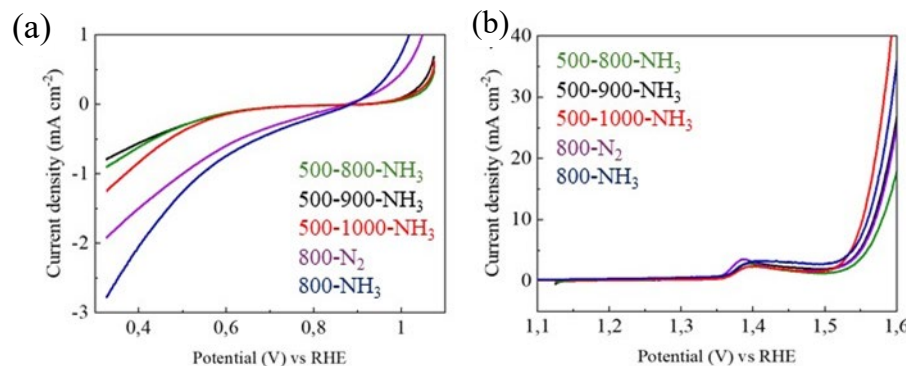
It can be seen that the 500-air sample exhibited XRD peaks corresponding to the lattice planes of anatase (TiO<sub>2</sub>) phase (JCPDS 00-021-1272, red), in agreement with the Raman results. The 500–800-NH<sub>3</sub>, 500–900-NH<sub>3</sub>, and 500–1000-NH<sub>3</sub> samples showed a combination of different phases as a consequence of the nitration provided by the NH<sub>3</sub> atmosphere and some kind of reduction conditions due to the presence of residual carbon. Conversion of anatase onto TiN was not complete, and the coexistence of titanium oxide (TiO; JCPDS 00-023-1078, violet) and osbonite–TiN (JCPDS 00-038-1420, black) was observed for the 500–800-NH<sub>3</sub>, 500–900-NH<sub>3</sub>, and 500–1000-NH<sub>3</sub> catalysts. In the diffractogram of the 500–800-NH<sub>3</sub> and 500–900-NH<sub>3</sub> catalysts, an additional phase assigned to titanium oxide nitride (JCPDS 00-044-0951) was also observed, probably due to the incomplete nitridation of the sample due to the presence of residual carbon [48]. The crystallite size of samples, which was calculated by the Debye–Scherrer equation from XRD patterns, increased with the temperature: 16.59, 21.08, and 39.41 nm after thermal treatment at 800, 900, and 1000 °C, respectively [48].

Figure 8 shows the XRD profiles of the samples 800-NH<sub>3</sub> and 800-N<sub>2</sub>. The crystallinity of the samples was lower than those that presented an intermediate treatment at 500 °C (Figure 7). The XRD spectra of the sample heat-treated at 800 °C in N<sub>2</sub> atmosphere revealed a pure crystallographic phase of anatase TiO<sub>2</sub> (JCPDS 00-021-1272). However, the sample treated at 800 °C in NH<sub>3</sub> indicated the existence of osbonite–TiN (JCPDS 00-038-1420) and titanium oxide (TiO; JCPDS 00-023-1078). The effect of the nitridation atmosphere at the same temperature on the powder phase composition showed that only NH<sub>3</sub> atmosphere can form cubic-phase TiN, indicating that it began to form. However, a small amount of TiO coexisted with the TiN phase due to the slow rate of the nitridation reaction [49].



**Figure 8.** X-ray diffraction patterns of 800-N<sub>2</sub> and 800-NH<sub>3</sub>. Assignments of the main phases detected are labeled.

Figure 9 shows the ORR and OER of the samples 500–800-NH<sub>3</sub>, 500–900-NH<sub>3</sub>, 500–1000-NH<sub>3</sub>, 800-N<sub>2</sub>, and 800-NH<sub>3</sub>.



**Figure 9.** (a) ORR and (b) OER of samples 500–800-NH<sub>3</sub>, 500–900-NH<sub>3</sub>, 500–1000-NH<sub>3</sub>, 800-N<sub>2</sub>, and 800-NH<sub>3</sub>.

A similar behavior of samples 500–800-NH<sub>3</sub>, 500–900-NH<sub>3</sub>, and 500–1000-NH<sub>3</sub> was observed for the ORR curves. However, the 800-N<sub>2</sub> and 800-NH<sub>3</sub> samples exhibited higher values of ORR current density than the samples with the additional treatment at 500 °C. This also occurred in the OER, except for the sample treated at 1000 °C. This improved behavior may be due to the higher porosity and surface area of the samples treated without the 500 °C intermediate step, which increases the contact between the electrode and electrolyte, favoring the oxidation and reduction of oxygen. Although the catalyst is well distributed over the nickel foam, if it also has a high surface area, contact with the aqueous electrolyte will increase, as it can penetrate the porosity of the catalyst. This improvement in the access of oxygen dissolved in the electrolyte to the surface of the catalyst significantly favors electrochemical reactions.

A balanced electrochemical behavior related to ORR and OER was achieved for the 800-NH<sub>3</sub> catalyst. To assess the electrocatalytic performance, cyclic voltammetry analysis was performed on the 800-NH<sub>3</sub> catalyst. The results, shown in Figure 10, indicate that the 800-NH<sub>3</sub> catalyst sample was active for both ORR and OER, with peaks of activity at 1.75 V and 1.95 V, respectively. Peaks observed at 1.35 V were associated with the formation of Ni complexes during the initial cycles of the test [24], and the reaction observed at 1.1 V corresponded to the HER, associated with the use of the Ti-based catalyst [14]. The increased intensity in the potential between 2.0 and 2.2 V is related to the degradation of

the electrolyte due to exceeding the stability potential of the aqueous electrolyte [8]. This sol-gel strategy allows for obtaining a bifunctional catalyst for ORR and OER reactions. DRX and Raman analyses showed a combination of the active anatase or sub-stoichiometric titanium oxides with the conductive titanium nitrides. The synergistic effect promoted by the coexistence of these active phases greatly enhanced the electronic conductivity. Other parameters also influenced the bifunctional activity; for example, the presence of N promoted the ORR and a large surface area, which enhanced good contact with the aqueous electrolyte and facilitated the access of oxygen dissolved in the electrolyte to the surface of the catalyst, significantly favoring both electrochemical reactions.

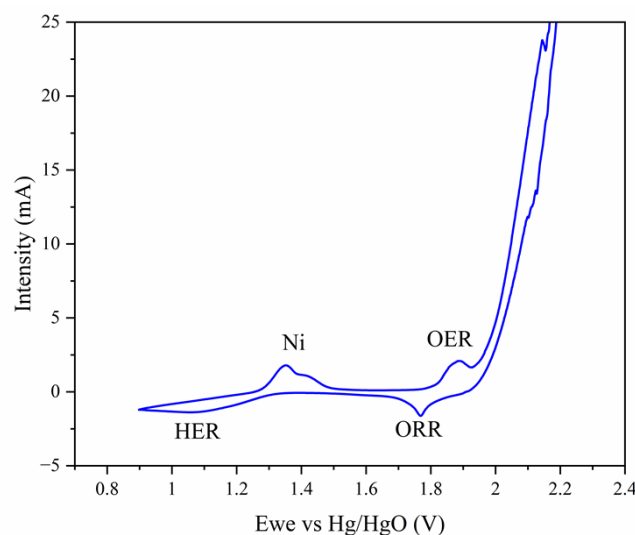


**Figure 10.** Cyclic voltammetry curve (cycle number 3) of 800-NH<sub>3</sub> supported on Ni foam (cathode) at a scan rate of 50 mV/min.

The study of the charge–discharge reversibility using the 800-NH<sub>3</sub> titanium-based catalyst and supported on nickel foam was carried out via galvanostatic charge–discharge tests (Figure 11). After the first discharge, where the surface oxidation of the Zn anode took place, the potential increased rapidly during charging until it reached a flat stage around 1.85 V, where the reduction of the Zn oxide-hydroxide occurred. After this stage, the charging process continued, increasing the potential until it stabilized at 1.93 V, where the water oxidation of the electrolyte took place, generating oxygen and protons [50]. This reaction is not part of the battery charging process and consumes aqueous electrolytes. To avoid this secondary reaction, the voltage was limited to 1.90 V to study only the charge–discharge process associated with the oxidation reduction of oxygen and zinc. From this point on, homogeneous discharge and charge cycles began to develop, as can be seen in the enlargement of Figure 11.

The discharge (ORR) included two plateaus centered at 1.7 and 1.5 V, possibly associated with the oxidation of the Zn anode to Zn(OH)<sub>4</sub><sup>2-</sup>, and later to ZnO [51]. However, the charging process took place in a single stage of longer duration centered around 1.84 V, where the OER associated with the reduction in Zn compounds took place. After numerous periods of charge–discharge, the cyclability of the cell was lost, placing the potential at 1.3 V, close to the open-circuit potential. Later, the results of the post-mortem study carried out on the cell electrodes after cycling will be shown. Figure 12 shows the results of the test under the same conditions, but without using a titanium-based catalyst in the cathode, i.e., using only the nickel foam to assess the effect of the titanium-based catalyst on the electrochemical behavior.

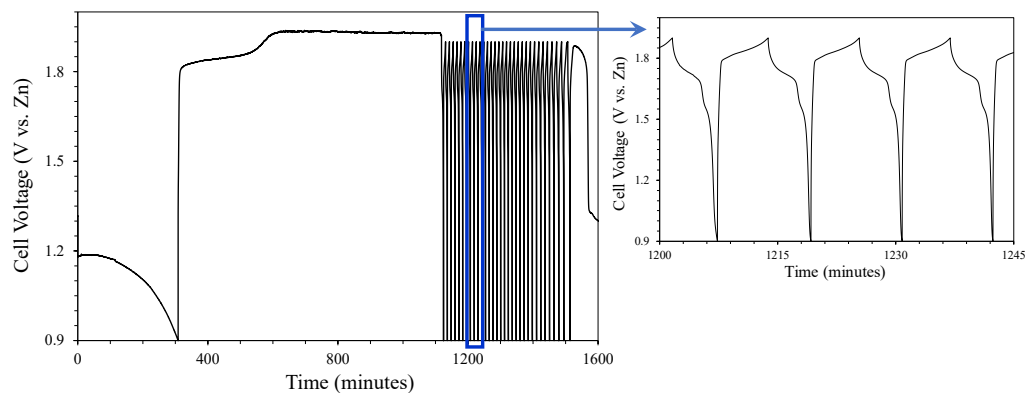


**Figure 11.** Galvanostatic charge–discharge test of the 800-NH<sub>3</sub> titanium-based sample supported on nickel foam (cathode).

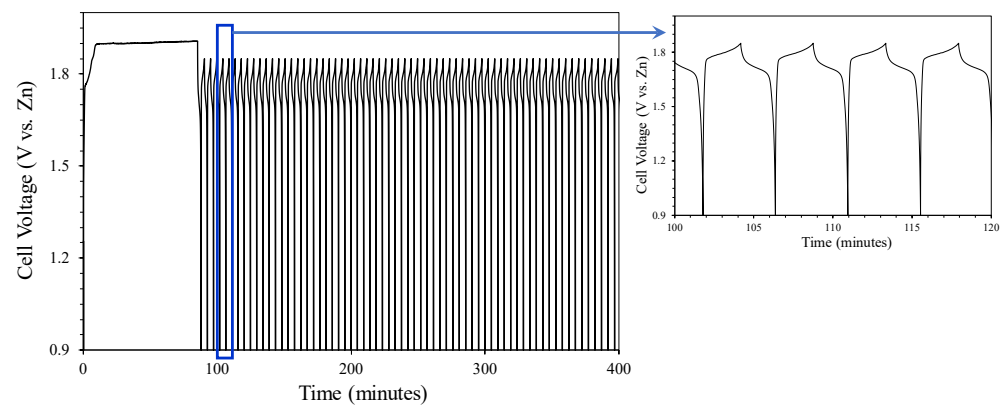


**Figure 12.** Galvanostatic charge–discharge test of nickel foam (cathode) without a catalyst.

As in the previous case, it was necessary to reduce the maximum potential of the charge–discharge test since the potential stabilized when the oxidation of the water electrolyte began. In this case, only one stage was observed in the discharge process, associated with ORR and centered at approximately 1.7 V. The charge stage associated with OER was centered at 1.8 V. The main difference in both types of tests was the duration of each charge–discharge cycle, which went from 4.6 min for the nickel foam cathode without a catalyst to 11.9 min when the titanium-based catalyst was incorporated into the nickel foam.

Figure 13 shows SEM images of the electrode surface (facing the electrolyte) after the charge–discharge test of the cell containing the titanium-based catalyst. The surface of the Zn anode after the test appeared completely covered with spherical precipitates of approximately 2 µm with intercalated porosity (Figure 13a).

Figure 13b,c present images at different magnifications of the nickel foam surface after cycling. Agglomerates of precipitates together with small filaments adhered to the nickel foam can be observed. The EDS analysis of these precipitates (Figure 13d) showed the presence of the constituent elements of the catalyst, but also K from the electrolyte and Zn that had diffused through the electrolyte and the separating membrane. Nitrogen was not observed in this analysis due to its low concentration in relation to titanium, the main component of the catalyst. The peaks associated with the nickel foam were not very intense because the analysis was carried out on an area with a high concentration of precipitates.

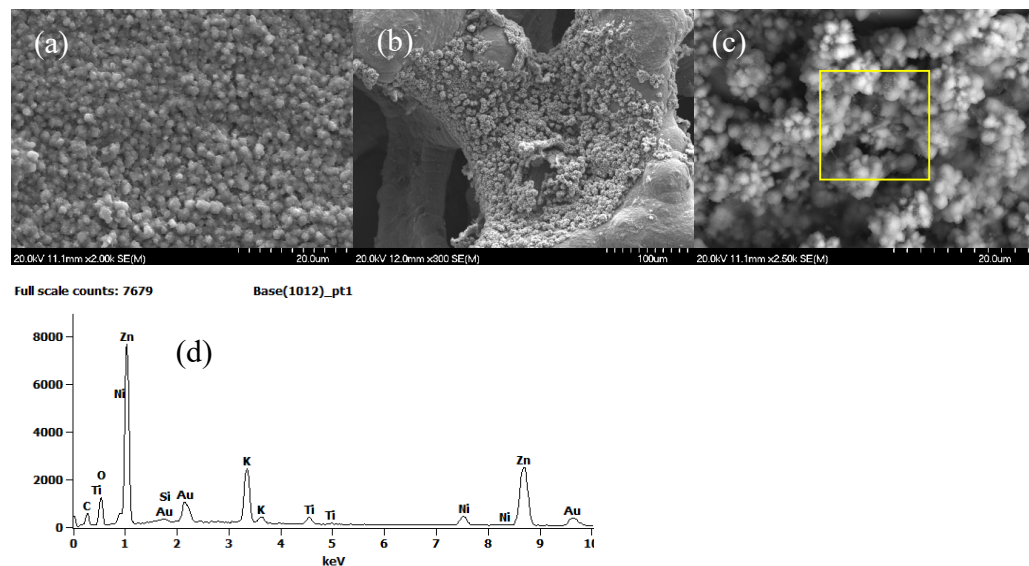


**Figure 13.** SEM images of both electrodes after the galvanostatic charge–discharge test with the 800- NH<sub>3</sub> titanium-based catalyst supported on nickel foam: (a) Zn anode, and (b,c) Ni foam cathode at two different magnifications. EDX analysis of (d) particles on Ni foam (marked square area).

The causes of the abrupt stoppage of cycling may be associated with three factors: (1) the continuous flow of oxygen extracted water from inside the cell, limiting the diffusion of ions between the electrodes, (2) the increasing passivation of the Zn foil surface with the number of cycles, and (3) the diffusion and subsequent precipitation of Zn ions into the cathode, which reduced the efficiency of the catalyst. These results guide the research that will soon be carried out, such as the control of oxygen flow to the cell, the design of a porous Zn anode that limits passivation, and the use of an alkaline electrode membrane (AEM) to restrict the ion diffusion between electrodes and hydroxyl groups.

#### 4. Conclusions

In summary, metal cathodes based on titanium nitrides were synthesized via the sol-gel method, in combination with surfactants, enabling us to efficiently obtain a nitride catalyst at low temperatures. It has been determined that the optimal treatment for obtaining a catalyst characterized by a high surface area and electric current is a pretreatment at 100 °C, followed by one at 800 °C in an ammonium atmosphere. The temperature and atmosphere of the heat treatments have been proven to be key factors that determine the electrochemical behavior of the synthesized catalysts.

The use of Ni foam as support provided a three-dimensional structure, allowing the presence of diffusion pathways that facilitate electron transfer and metal ions' diffusion, and air.

The synthesized materials showed the capacity to perform multiple galvanostatic charge–discharge cycles. The tests were performed using metallic Zn as an anode in an aqueous solution and showed no signs of chemical or structural instability throughout the cycles performed. However, the capacity of these materials as batteries is limited by the stability of water as an electrolyte, since at voltages exceeding or approaching 1.9 V, it will destabilize and prevent the charge–discharge cycles. Titanium nitride cathodes showed high ORR and OER values, indicating that these types of cathodes are promising fields of study for metal-air batteries in aqueous media. Additionally, they presented a high number of cycles, indicating good reversibility.

At present, the cathodes for metal-air batteries are overwhelmingly carbon-based since they have a considerable catalytic capacity and a good conductive additive. However, they present a series of problems that reduce their stability and the ability to maintain the capacity and reversibility that a battery requires for its proper operation. This is the reason

why the study of techniques for the assembly and study of batteries in nickel foams with metallic cathodes presents a high interest. It is to be expected that in the short–medium term, more studies with different prototypes or tests in metal-air batteries will appear, paving the way for the future industrialization of the use of batteries with an energy density much higher than the present ones.

**Author Contributions:** Conceptualization, J.M., N.C.R.-N., A.M., K.T. and M.A.; methodology, J.G.-M., J.M., S.I., N.C.R.-N., A.M., K.T. and M.A.; validation, J.M., N.C.R.-N., A.M., K.T. and M.A.; formal analysis, J.M., N.C.R.-N., A.M., K.T. and M.A.; investigation, J.G.-M., J.M., S.I., N.C.R.-N., A.M., K.T. and M.A.; resources, J.M. and M.A.; data curation, J.M., N.C.R.-N., A.M., K.T. and M.A.; writing—original draft preparation, J.G.-M., J.M. and M.A.; writing—review and editing, J.G.-M., J.M., S.I., N.C.R.-N., A.M., K.T. and M.A.; visualization, J.G.-M., J.M. and M.A.; supervision, J.M. and M.A.; project administration, K.T. and M.A.; funding acquisition, K.T. and M.A. All authors have read and agreed to the published version of the manuscript.

**Funding:** This research was funded by the project “Novel carbon-free cathode materials for metal-air rechargeable batteries (CarFree)”, of the program Horizon 2020-JST to Fund 5 Projects in EIG CONCERT-Japan, within the Framework of the Strategic International Collaborative Research Program (SICORP). Proyecto de colaboración internacional MICIN PCI2018-092982.

**Data Availability Statement:** Data available on request due to restrictions eg privacy or ethical.

**Acknowledgments:** J.G.-M. thanks the predoctoral contract “Garantía Juvenil” of the Comunidad de Madrid (grant number CAM19\_PRE\_ICV\_002), and J.M. thanks CSIC for the PIE i3-2022 project.

**Conflicts of Interest:** The authors declare no conflicts of interest.

## References

1. Zhang, X.; Wang, Y.-P.; Rayner, P.J.; Ciais, P.; Huang, K.; Luo, Y.; Piao, S.; Wang, Z.; Xia, J.; Zhao, W.; et al. A small climate-amplifying effect of climate–carbon cycle feedback. *Nat. Commun.* **2021**, *12*, 2952. [[CrossRef](#)]
2. Kravtsev, A.; Ein-Eli, Y. Review on Li–air batteries—Opportunities, limitations and perspective. *J. Power Sources* **2011**, *196*, 886–893. [[CrossRef](#)]
3. Nitta, N.; Wu, F.; Lee, J.T.; Yushin, G. Li-ion battery materials: Present and future. *Mater. Today* **2015**, *18*, 252–264. [[CrossRef](#)]
4. Lee, J.-S.; Kim, S.T.; Cao, R.; Choi, N.-S.; Liu, M.; Lee, K.T.; Cho, J. Metal-Air Batteries with High Energy Density: Li-Air versus Zn-Air. *Adv. Energy Mater.* **2011**, *1*, 34–50. [[CrossRef](#)]
5. Wang, K.; Yu, J. Lifetime simulation of rechargeable zinc-air battery based on electrode aging. *Energy Storage* **2020**, *28*, 101191. [[CrossRef](#)]
6. Pan, J.; Tian, X.L.; Zaman, S.; Dong, Z.; Liu, H.; Park, H.S.; Xia, B.Y. Recent Progress on Transition Metal Oxides as Bifunctional Catalysts for Lithium-Air and Zinc-Air Batteries. *Batter. Supercaps* **2018**, *2*, 336–347. [[CrossRef](#)]
7. Wang, Q.; Kaushik, S.; Xiao, X.; Xu, Q. Sustainable zinc–air battery chemistry: Advances, challenges and prospects. *Chem. Soc. Rev.* **2023**, *52*, 6139–6190. [[CrossRef](#)] [[PubMed](#)]
8. Guo, H.; Luo, W.; Chen, J.; Chou, S.; Liu, H.; Wang, J. Review of Electrolytes in Nonaqueous Lithium–Oxygen Batteries. *Adv. Sustain. Syst.* **2018**, *2*, 1700183. [[CrossRef](#)]
9. Zeng, X.; Hao, J.; Wang, Z.; Mao, J.; Guo, Z. Recent progress and perspectives on aqueous Zn-based rechargeable batteries with mild aqueous electrolytes. *Energy Storage Mater.* **2019**, *20*, 410–437. [[CrossRef](#)]
10. Cang, R.; Ye, K.; Zhu, K.; Yan, J.; Yin, J.; Cheng, K.; Wang, G.; Cao, D. Organic 3D interconnected graphene aerogel as cathode materials for high-performance aqueous zinc ion battery. *J. Energy Chem.* **2020**, *45*, 52–58. [[CrossRef](#)]
11. Liang, Y.; Lei, H.; Wang, S.; Wang, Z.; Mai, W. Pt/Zn heterostructure as efficient air-electrocatalyst for long-life neutral Zn-air batteries. *Sci. China Mater.* **2021**, *64*, 1868–1875. [[CrossRef](#)]
12. Pan, J.; Xu, Y.Y.; Yang, H.; Dong, Z.; Liu, H.; Xia, B.Y. Advanced Architectures and Relatives of Air Electrodes in Zn–Air Batteries. *Adv. Sci.* **2018**, *5*, 1700691. [[CrossRef](#)] [[PubMed](#)]
13. Li, Y.; Dai, H. Recent advances in zinc–air batteries. *Chem. Soc. Rev.* **2014**, *43*, 5257–5275. [[CrossRef](#)] [[PubMed](#)]
14. Liu, Q.; Pan, Z.; Wang, E.; An, L.; Sun, G. Aqueous metal-air batteries: Fundamentals and applications. *Energy Storage Mater.* **2019**, *27*, 478–505. [[CrossRef](#)]
15. Wang, Z.-L.; Xu, D.; Xu, J.-J.; Zhang, X.-B. Oxygen electrocatalysts in metal–air batteries: From aqueous to nonaqueous electrolytes. *Chem. Soc. Rev.* **2014**, *43*, 7746–7786. [[CrossRef](#)]
16. Wang, H.; Tan, R.; Yang, Z.; Feng, Y.; Duan, X.; Ma, J. Stabilization Perspective on Metal Anodes for Aqueous Batteries. *Adv. Energy Mater.* **2021**, *11*, 2000962. [[CrossRef](#)]
17. Fang, W.; Hu, H.; Jiang, T.; Li, G.; Wu, M. N- and S-doped porous carbon decorated with in-situ synthesized Co–Ni bimetallic sulfides particles: A cathode catalyst of rechargeable Zn-air batteries. *Carbon* **2019**, *146*, 476–485. [[CrossRef](#)]

18. Cano, Z.P.; Park, M.G.; Lee, D.U.; Fu, J.; Liu, H.; Fowler, M.; Chen, Z. New Interpretation of the Performance of Nickel-Based Air Electrodes for Rechargeable Zinc–Air Batteries. *J. Phys. Chem. C* **2018**, *122*, 20153–20166. [[CrossRef](#)]
19. Borchers, N.; Clark, S.; Horstmann, B.; Jayasayee, K.; Juel, M.; Stevens, P. Innovative zinc-based batteries. *J. Power Sources* **2021**, *484*, 229309. [[CrossRef](#)]
20. Kim, C.; Buonsanti, R.; Yaylian, R.; Milliron, D.J.; Cabana, J. Carbon-Free  $\text{TiO}_2$  Battery Electrodes Enabled by Morphological Control at the Nanoscale. *Adv. Energy Mater.* **2013**, *3*, 1286–1291. [[CrossRef](#)]
21. Ha, D.-H.; Islam, M.A.; Robinson, R.D. Binder-Free and Carbon-Free Nanoparticle Batteries: A Method for Nanoparticle Electrodes without Polymeric Binders or Carbon Black. *Nano Lett.* **2012**, *12*, 5122–5130. [[CrossRef](#)]
22. Liu, W.-M.; Yin, W.-W.; Ding, F.; Sang, L.; Fu, Z.-W.  $\text{NiCo}_2\text{O}_4$  nanosheets supported on Ni foam for rechargeable nonaqueous sodium-air batteries. *Electrochim. Commun.* **2014**, *45*, 87–90. [[CrossRef](#)]
23. Zheng, X.; Cao, X.; Zeng, K.; Sun, Z.; Yan, J.; Li, X.; Jin, C.; Chen, X.; Yang, R. Cotton pad-derived large-area 3D N-doped graphene-like full carbon cathode with an O-rich functional group for flexible all solid Zn–air batteries. *J. Mater. Chem. A* **2020**, *8*, 11202–11209. [[CrossRef](#)]
24. Jin, W.; Chen, J.; Liu, B.; Hu, J.; Wu, Z.; Cai, W.; Fu, G. Oxygen Vacancy–Rich In-Doped  $\text{CoO}/\text{CoP}$  Heterostructure as an Effective Air Cathode for Rechargeable Zn–Air Batteries. *Small* **2019**, *15*, e1904210. [[CrossRef](#)]
25. Davari, E.; Ivey, D.G. Synthesis and electrochemical performance of manganese nitride as an oxygen reduction and oxygen evolution catalyst for zinc–air secondary batteries. *J. Appl. Electrochem.* **2017**, *47*, 815–827. [[CrossRef](#)]
26. Wang, H.; Yu, H.; Yin, S.; Xu, Y.; Li, X.; Xue, H.; Wang, L. Integrated Mesoporous PtPd Film/Ni Foam: An Efficient Binder-Free Cathode for Zn–Air Batteries. *ACS Sustain. Chem. Eng.* **2018**, *6*, 12367–12374. [[CrossRef](#)]
27. Wan, L.; Zhao, Z.; Chen, X.; Liu, P.-F.; Wang, P.; Xu, Z.; Lin, Y.; Wang, B. Controlled Synthesis of Bifunctional  $\text{NiCo}_2\text{O}_4@\text{FeNi}$  LDH Core–Shell Nanoarray Air Electrodes for Rechargeable Zinc–Air Batteries. *ACS Sustain. Chem. Eng.* **2020**, *8*, 11079–11087. [[CrossRef](#)]
28. Ma, T.Y.; Cao, J.L.; Jaroniec, M.; Qiao, S.Z. Interacting Carbon Nitride and Titanium Carbide Nanosheets for High-Performance Oxygen Evolution. *Angew. Chem.* **2016**, *128*, 1150–1154. [[CrossRef](#)]
29. Cai, X.; Lai, L.; Lin, J.; Shen, Z. Recent advances in air electrodes for Zn–air batteries: Electrocatalysis and structural design. *Mater. Horiz.* **2017**, *4*, 945–976. [[CrossRef](#)]
30. Rebrov, E.V.; Gao, P.-Z. Molecular Catalysts for OER/ORR in Zn–Air Batteries. *Catalysts* **2023**, *13*, 1289. [[CrossRef](#)]
31. Xu, C.; Niu, Y.; Au, V.K.-M.; Gong, S.; Liu, X.; Wang, J.; Wu, D.; Chen, Z. Recent progress of self-supported air electrodes for flexible Zn-air batteries. *J. Energy Chem.* **2024**, *89*, 110–136. [[CrossRef](#)]
32. Zhang, S.; Chen, M.; Zhao, X.; Cai, J.; Yan, W.; Yen, J.C.; Chen, S.; Yu, Y.; Zhang, J. Advanced Noncarbon Materials as Catalyst Supports and Non-noble Electrocatalysts for Fuel Cells and Metal–Air Batteries. *Electrochim. Energy Rev.* **2021**, *4*, 336–381. [[CrossRef](#)]
33. Liu, F.; Yang, X.; Dang, D.; Tian, X. Engineering of Hierarchical and Three-Dimensional Architectures Constructed by Titanium Nitride Nanowire Assemblies for Efficient Electrocatalysis. *ChemElectroChem* **2019**, *6*, 2208–2214. [[CrossRef](#)]
34. Kim, B.G.; Jo, C.; Shin, J.; Mun, Y.; Lee, J.; Choi, J.W. Ordered Mesoporous Titanium Nitride as a Promising Carbon-Free Cathode for Aprotic Lithium–Oxygen Batteries. *ACS Nano* **2017**, *11*, 1736–1746. [[CrossRef](#)] [[PubMed](#)]
35. Deng, D.-R.; An, T.-H.; Li, Y.-J.; Wu, Q.-H.; Zheng, M.-S.; Dong, Q.-F. Hollow porous titanium nitride tubes as a cathode electrode for extremely stable Li–S batteries. *J. Mater. Chem. A* **2016**, *4*, 16184–16190. [[CrossRef](#)]
36. Hubbard, D.; Nuruddin, M.; Tcherbi-Narteh, A.; Hosur, M.; Jeelani, S. In Proceedings of the CAMX 2015–Composites and Advanced Materials Expo 2015, Dallas, TX, USA, 27–29 October 2015; pp. 122–135.
37. Choi, D.; Kumta, P.N. Synthesis of Nanostructured TiN Using a Two-Step Transition MetalHalide Approach. *J. Am. Ceram. Soc.* **2005**, *88*, 2030–2035. [[CrossRef](#)]
38. Zhang, D.; Zheng, L.; Ma, Y.; Lei, L.; Li, Q.; Li, Y.; Luo, H.; Feng, H.; Hao, Y. Synthesis of Nitrogen- and Sulfur-Codoped 3D Cubic-Ordered Mesoporous Carbon with Superior Performance in Supercapacitors. *ACS Appl. Mater. Interfaces* **2014**, *6*, 2657–2665. [[CrossRef](#)] [[PubMed](#)]
39. Ismagilov, Z.R.; Shalagina, A.E.; Podyacheva, O.Y.; Ischenko, A.V.; Kibis, L.S.; Boronin, A.I.; Chesalov, Y.A.; Kochubey, D.I.; Romanenko, A.I.; Anikeeva, O.B.; et al. Structure and electrical conductivity of nitrogen-doped carbon nanofibers. *Carbon* **2009**, *47*, 1922–1929. [[CrossRef](#)]
40. Choi, D.; Kumta, P.N. Nanocrystalline TiN Derived by a Two-Step Halide Approach for Electrochemical Capacitors. *J. Electrochem. Soc.* **2006**, *153*, A2298–A2303. [[CrossRef](#)]
41. Delegan, N.; Daghrir, R.; Drogui, P.; El Khakani, M.A. Bandgap tailoring of *in-situ* nitrogen-doped  $\text{TiO}_2$  sputtered films intended for electrophotocatalytic applications under solar light. *J. Appl. Phys.* **2014**, *116*, 153510. [[CrossRef](#)]
42. Bagheri, S.; Shameli, K.; Abd Hamid, S.B. Synthesis and Characterization of Anatase Titanium Dioxide Nanoparticles Using Egg White Solution via Sol-Gel Method. *J. Chem.* **2013**, *2013*, 848205. [[CrossRef](#)]
43. Čolović, B.; Kisić, D.; Jokanović, B.; Rakočević, Z.; Nasov, I.; Petkoska, A.T.; Jokanović, V. Wetting properties of titanium oxides, oxynitrides and nitrides obtained by DC and pulsed magnetron sputtering and cathodic arc evaporation. *Mater. Sci.* **2019**, *37*, 173–181. [[CrossRef](#)]
44. Zhao, F.; Xue, X.; Fu, W.; Liu, Y.; Ling, Y.; Zhang, Z. TiN Nanorods as Effective Substrate for Surface-Enhanced Raman Scattering. *J. Phys. Chem. C* **2019**, *123*, 29353–29359. [[CrossRef](#)]

45. Nishikiori, H.; Takei, M.; Oki, K.; Takano, S.; Tanaka, N.; Fujii, T. Photocatalytic activity of titania layer prepared by oxidizing titanium compounds on titanium plate surface. *Appl. Catal. B Environ.* **2012**, *127*, 227–233. [[CrossRef](#)]
46. Wei, H.; Wu, M.; Dong, Z.; Chen, Y.; Bu, J.; Lin, J.; Yu, Y.; Wei, Y.; Cui, Y.; Wang, R. Composition, microstructure and SERS properties of titanium nitride thin film prepared via nitridation of sol–gel derived titania thin films. *J. Raman Spectrosc.* **2017**, *48*, 578–585. [[CrossRef](#)]
47. Zhu, S.; Xiao, L.; Cortie, M. Surface enhanced Raman spectroscopy on metal nitride thin films. *Vib. Spectrosc.* **2016**, *85*, 146–148. [[CrossRef](#)]
48. Ma, Y.; Nagai, T.; Inoue, Y.; Ikegami, K.; Kuroda, Y.; Matsuzawa, K.; Napporn, T.W.; Liu, Y.; Mitsushima, S.; Ishihara, A. Control of surface area and conductivity of niobium-added titanium oxides as durable supports for cathode of polymer electrolyte fuel cells. *Mater. Des.* **2021**, *203*, 109623. [[CrossRef](#)]
49. Li, J.; Gao, L.; Sun, J.; Zhang, Q.; Guo, J.; Yan, D. Synthesis of Nanocrystalline Titanium Nitride Powders by Direct Nitridation of Titanium Oxide. *J. Am. Ceram. Soc.* **2001**, *84*, 3045–3047. [[CrossRef](#)]
50. Vany, P. CRC Handbook of Chemistry and Physics, 97th ed.; CRC Press: Boca Ratón, FL, USA, 2016.
51. Stumpf, M.; Damtew, D.; Stock, D.; Hess, K.; Schröder, D.; Schlettwein, D. Controlled Electrodeposition of Zinc Oxide on Conductive Meshes and Foams Enabling Its Use as Secondary Anode. *J. Electrochem. Soc.* **2018**, *165*, D461–D466. [[CrossRef](#)]

**Disclaimer/Publisher’s Note:** The statements, opinions and data contained in all publications are solely those of the individual author(s) and contributor(s) and not of MDPI and/or the editor(s). MDPI and/or the editor(s) disclaim responsibility for any injury to people or property resulting from any ideas, methods, instructions or products referred to in the content.